An aerogel Cherenkov detector for multi-GeV photon detection with low sensitivity to neutrons

AUTHOR(S):

Maeda, Y.; Kawasaki, N.; Masuda, T.; Morii, H.; Naito, D.; Nakajima, Y.; Nanjo, H.; ... Shiomi, K.; Sumida, T.; Tajima, Y.

CITATION:

Maeda, Y. ...[et al]. An aerogel Cherenkov detector for multi-GeV photon detection with low sensitivity to neutrons. Progress of Theoretical and Experimental Physics 2015, 2015(6): 63H01.

ISSUE DATE:

2015-06-01

URL:

http://hdl.handle.net/2433/202886

PTEP
Prog. Theor. Exp. Phys. **2015**, 063H01 (16 pages)
DOI: 10.1093/ptep/ptv074

An aerogel Cherenkov detector for multi-GeV photon detection with low sensitivity to neutrons

Y. Maeda[1,*], N. Kawasaki[1], T. Masuda[1,†], H. Morii[1], D. Naito[1], Y. Nakajima[1,‡], H. Nanjo[1], T. Nomura[2], N. Sasao[3], S. Seki[1], K. Shiomi[4,§], T. Sumida[1], and Y. Tajima[5]

[1]*Department of Physics, Kyoto University, Kyoto 606-8502, Japan*
[2]*Institute of Particle and Nuclear Studies, High Energy Accelerator Research Organization (KEK), Tsukuba, Ibaraki 305-0801, Japan*
[3]*Research Core for Extreme Quantum World, Okayama University, Okayama 700-8530, Japan*
[4]*Department of Physics, Osaka University, Toyonaka, Osaka 560-0045, Japan*
[5]*Department of Physics, Yamagata University, Yamagata 990-8560, Japan*
*E-mail: maeda_y@scphys.kyoto-u.ac.jp

Received December 23, 2014; Revised April 21, 2015; Accepted April 29, 2015; Published June 16, 2015

We describe a novel multi-GeV photon detector which operates under an intense flux of neutrons. It is composed of lead–aerogel sandwich counter modules. Its salient features are high photon detection efficiency and blindness to neutrons. Monte Carlo (MC) simulations show that the efficiency for photons with energy larger than 1 GeV is expected to be higher than 99.5% and that for 2 GeV/c neutrons is less than 1%. Performance of photon detection with an underlying large flux of neutrons was measured by a partial detector with 12 modules. We confirm the efficiency for photons with energy >1 GeV is consistent with the MC expectation within an uncertainty of 8.2%.

Subject Index C30, H14

1. Introduction

Electromagnetic sampling calorimeters are among the most popular detectors for detecting photons in high energy physics. They are usually composed of alternate layers of high-Z converters and active materials sensitive to electrons and positrons. Incident photons produce electromagnetic showers in the converter layers and their energies are measured in the active layers.

In this paper, we describe a novel photon detector with lead–aerogel layers operating within an environment with an underlying intense flux of neutrons. We choose Cherenkov radiation emitted from an aerogel medium since this process allows the detector to be sensitive to electrons/positrons and not to neutrons. The detector is being used in a rare K_L decay experiment [1,2] at the J-PARC Main Ring (MR) [3]. The experiment, named KOTO, aims to observe the CP-violating decay mode of $K_L \to \pi^0\nu\bar{\nu}$ with a sensitivity exceeding the standard model prediction ($Br \simeq (2.4 \pm 0.4) \times 10^{-11}$ [4]). An intense neutral kaon beam is needed to achieve the sensitivity. The beam contains large fluxes of photons, neutrons, and K_Ls with typical energies of 10 MeV, 1.4 GeV, and 2 GeV, respectively.

[†]Present address: Research Core for Extreme Quantum World, Okayama University, Okayama 700-8530, Japan.
[‡]Present address: Lawrence Berkeley National Laboratory, Berkeley, California 94720, USA.
[§]Present address: Institute of Particle and Nuclear Studies, High Energy Accelerator Research Organization (KEK), Tsukuba, Ibaraki 305-0801, Japan.

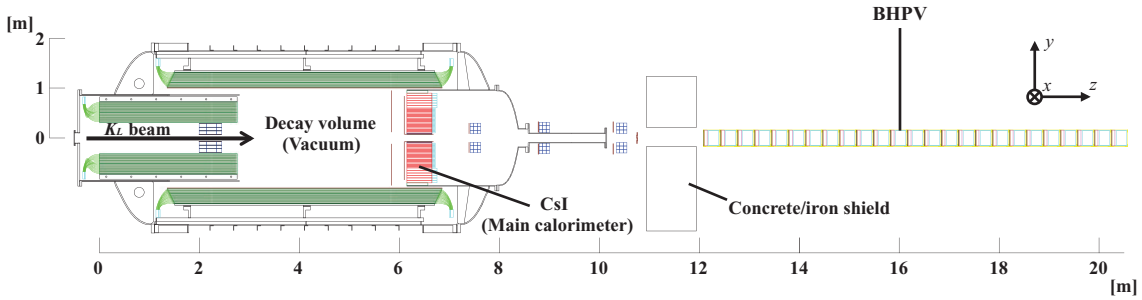

Fig. 1. Schematic cross-sectional view of the KOTO detector assembly.

Rates of the photons and neutrons are expected to be approximately 600 MHz each with the designed beam condition. Figure 1 shows a cross-sectional view of the KOTO detector assembly. The signature of the $K_L \to \pi^0\nu\bar{\nu}$ decay is a pair of photons from π^0 and no other visible particles. The two photons from the π^0 are detected with an electromagnetic calorimeter (CsI in Fig. 1) placed downstream of the decay volume. A number of veto counters surrounding the decay volume hermitically ensure that no other particle is detected at the same time. The major background is expected to come from the decay $K_L \to 2\pi^0 \to 4\gamma$, in which two out of the four photons escape detection. In order to suppress this background, photon detection with high efficiency is essential. This requirement is also true for photons escaping in the beam direction. The energies of these photons range between 100 MeV and 5 GeV. Thus, an efficient photon detector to work within the beam with an underlying large flux of neutrons is needed. The crucial feature for a photon detector to be used in a very intense beam is neutron blindness, to reduce single counting rates and overveto probabilities of signal events. Various requirements on the detector, particularly the following, were evaluated by Monte Carlo (MC) simulations:

- Efficiency > 99.5% for photons with energies of 1 GeV or greater;
- Efficiency < 1% for neutrons with momentum of 2 GeV/c.

In Sect. 2, we report various design studies to satisfy these requirements, including results of test experiments with positron and proton beams for verification of the detector response and tuning of the simulation. In Sect. 3, the performance on photon detection in the neutral beam was evaluated for the partially installed detector in the KOTO experimental area. The appendix describes the measurement of the transmittance of the aerogel radiators, which provided important parameters concerning the light yield.

2. Design and expected performance

We explain the basic concepts of the detector with a description of its components. Next, we report the results of two test experiments with positrons and protons. Finally, we present the results of simulation studies on the performance of the designed detector.

2.1. Basic design

The detector, named BHPV (Beam Hole Photon Veto), is placed at the most downstream part of the KOTO detector assembly as shown in Fig. 1. It is composed of 25 layers of modules along the beam. The structure of a single module is shown in Fig. 2. The main part of the module consists of a lead converter and an aerogel radiator as well as light-collecting mirrors and photomultiplier tubes (PMTs).

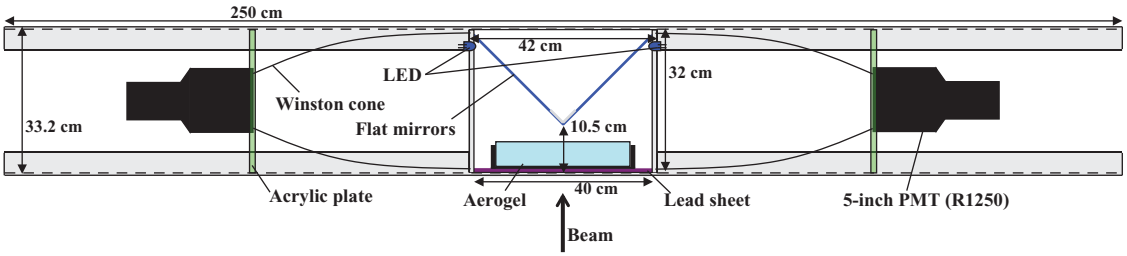

Fig. 2. Diagram of a single module (top view).

Design concepts. Photons are detected through Cherenkov radiation of the converted electrons and positrons in the aerogel, which is known to have a small index of refraction in the range 1.007–1.13. This method enables us to reduce sensitivity to neutrons since they tend to produce slower particles which yield less Cherenkov light than $e^{\pm}$.

In order to achieve high photon efficiency, optimizations of the thicknesses of the converter and radiator and of the refractive index of the aerogel are important. In general, a large number of samplings are required because each converter should be thin enough to reduce the stopping of shower particles inside the converter, and the total thickness should be large enough to ensure conversion of photons into showers. In our case, a total converter thickness of 10 X_0 and 25 samplings were adopted, where the number of samplings was maximized within the available space while keeping a 99.9% conversion probability of incident photons. The refractive index of aerogel was chosen as $n = 1.03$ by optimizing the photon efficiency and neutron blindness. The detector performance was found to be insensitive to the specific index value from simulation studies.

The arrayed configuration along the beam has the additional merit of reducing neutron sensitivity. We note that electromagnetic showers from high-energy photons tend to develop in the forward direction, while secondary particles such as protons and pions produced by neutron interactions have more isotropic angular distributions. By defining photons as events with hits in three or more consecutive modules, we remove a substantial fraction of the neutron events. Contributions from photons with energies less than 50 MeV in the beam can also be reduced by this requirement. Quantitative results of the studies, performed with MC simulations, can be found in Sect. 2.4.

Structure of a single module. Each single module consists of a lead sheet and aerogel tiles followed by a light-collection system and PMTs. The thickness of the lead sheet is either 1.5 or 3.0 mm, depending on the modules. Two types of aerogel tiles with different sizes and optical qualities are used. They are named type-M and type-A, as listed in Table 1. The type-M aerogel was purchased from Matsushita Electric Works, Ltd.,[1] and the type-A was originally produced for the KEK E248(AIDA) experiment [5]. Several layers of type-M (type-A) tiles are arranged in a 3×3 (2×2) grid to cover a transverse size of 300 mm^2, larger than the actual neutral beam of 200 mm^2 to detect diverging photons from K_L decays. These tiles are wrapped with a thin polyvinylidene chloride sheet, with a visible light transmittance of 90%. The sheet serves to maintain the aerogel rigidity. The optical system has two identical arms, each of which consists of a flat mirror, a Winston cone [7] for collecting light, and a 5 inch PMT. The advantages of the dual readout system include efficient and uniform light collection. In addition, single counting rates are cut in half, alleviating possible

[1] Presently Panasonic Corporation, 1006, Oaza Kadoma, Kadoma-shi, Osaka 571-8501, Japan.

Table 1. Parameters of the aerogel radiators. Type-M tiles were used in the calibration measurement (Sect. 2.2) and type-A were used in the simulation study (Sect. 2.4) and the physics run (Sect. 3). The refractive index was measured with the Fraunhofer method [6].

Type	Refractive index† (n)	Dimensions [mm^3]	Configuration of stacking	Transmission length* [cm] (at the wavelength of 400 nm)
M	1.031	$100 \times 100 \times 11$	3×3	5.07
A	1.028	$159 \times 159 \times 29$	2×2	3.35

*The transmission length, defined as the path length at which the original intensity is reduced to $1/e$, is calculated with Eq. (1) using the measured parameters. See the appendix for details.
†The refractive index was treated as $n = 1.03$ for both types of aerogel in the simulations.

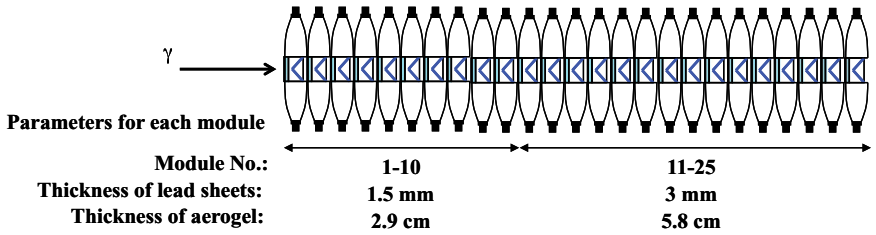

Fig. 3. Layout of the BHPV detector.

performance deterioration under high rate operation. The flat mirror is made of a 0.75 mm-thick aluminum sheet coated by an anodizing method. The reflectivity is 85% over the visible light region. The Winston cone (480 mm long) is designed to funnel the Cherenkov light from the input aperture of 300 mm in diameter into the output aperture of 120 mm. It is made of aluminum sheet with deep-draw processing.[2] The cone inner surface is coated with aluminum by vapor deposition. The average reflectivity is 85% for visible light. The 5 inch PMT, Hamamastu R1250,[3] has a bialkali photocathode with borosilicate glass. Its quantum efficiency peaks around the wavelength of 400 nm with a value of 20%, according to catalog information. Light emitting diodes (LEDs) are installed for calibration of the PMTs.

Configuration of modules. Twenty-five modules are arranged along the beam axis. The thickness of the lead and aerogel radiator for each module are shown in Fig. 3. This configuration, used in the simulation studies described in Sect. 2.4, is referred to as the reference configuration. It is optimized with respect to experimental conditions including beam intensity in order to maintain high photon detection efficiency and low single counting rates. For example, the thinner lead sheets and aerogel in the upstream modules help to reduce the counting rates in these modules where high rates are expected.

2.2. *Photoelectron yield measurement with a positron beam*

The average number of observed photoelectrons (p.e.) produced by a single relativistic electron traveling through the aerogel radiator is the most important quantity. The value was obtained by the

[2] Manufactured by Yokohama Kiko Co., Ltd., 2-11-1, Fukuura, Kanazawa-ku, Yokohama-shi, Kanagawa, 236-8647, Japan.
[3] Hamamatsu Photonics K.K., http://www.hamamatsu.com/jp/en/R1250.html, date last accessed May 21, 2015.

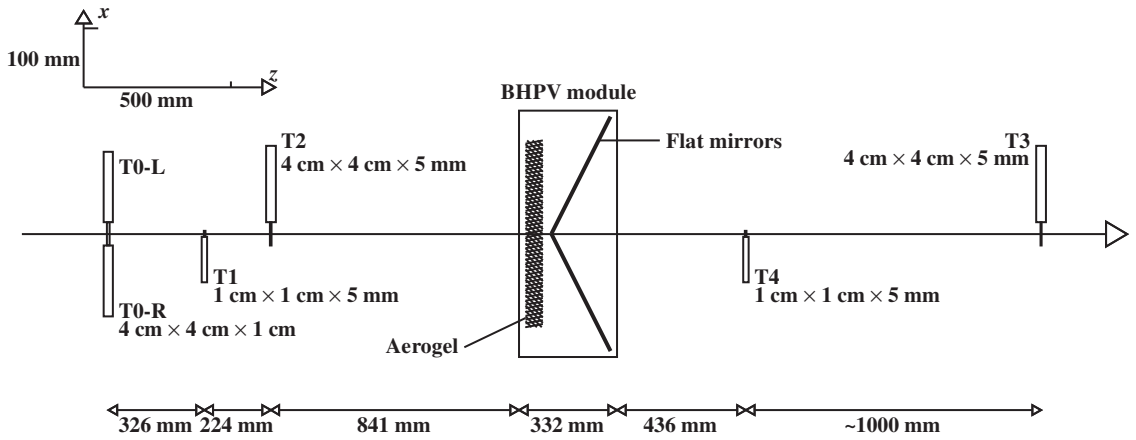

Fig. 4. Layout of the photoelectron calibration measurements using positrons. The z-axis indicates the beam direction. The name and size are shown for each trigger counter. Only part of the BHPV detector module including the aerogel radiator and flat mirrors is drawn for simplicity (see Fig. 2 for the optical system). The lead converter was not inserted for this measurement.

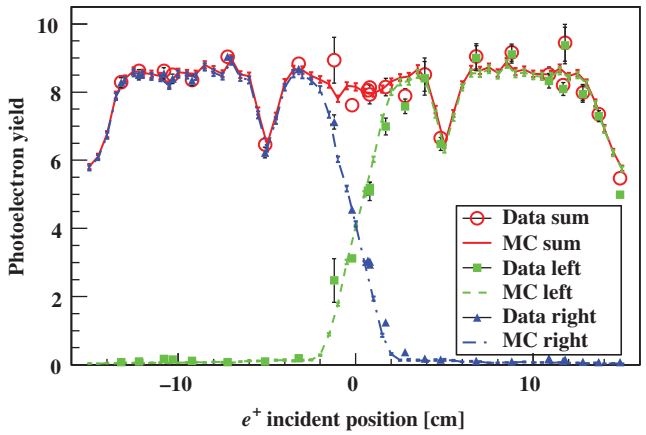

Fig. 5. The data (markers) and MC simulation results (lines) of light yields as a function of the horizontal (x) position of the positron (e^+) beam. The green and blue colors indicate outputs from the PMTs at the left and the right side, respectively, and the red indicates the sum of the two PMTs.

"calibration experiment" with a positron beam. The experiment was performed with a 600 MeV/c positron beam at the Laboratory of Nuclear Science[4] of Tohoku University, Japan in 2009. Five layers of type-M aerogel tiles were used. Figure 4 shows a schematic view of the experimental layout. Plastic scintillation counters were placed both upstream and downstream of the detector module. The trigger signal was formed by the coincidence signals of the T1 and T4 counters. Both counters had dimensions of 1 cm × 1 cm in cross section and 0.5 cm in thickness.

Figure 5 shows the photoelectron yields as a function of the horizontal beam position. The output of each PMT was converted to the number of photoelectrons using one-photoelectron peaks from LED calibration data. The results of corresponding GEANT4 [8] MC simulations are shown in the same figure with lines, where ray tracing was performed for individual Cherenkov light produced

[4] Presently the Research Center for Electron Photon Science.

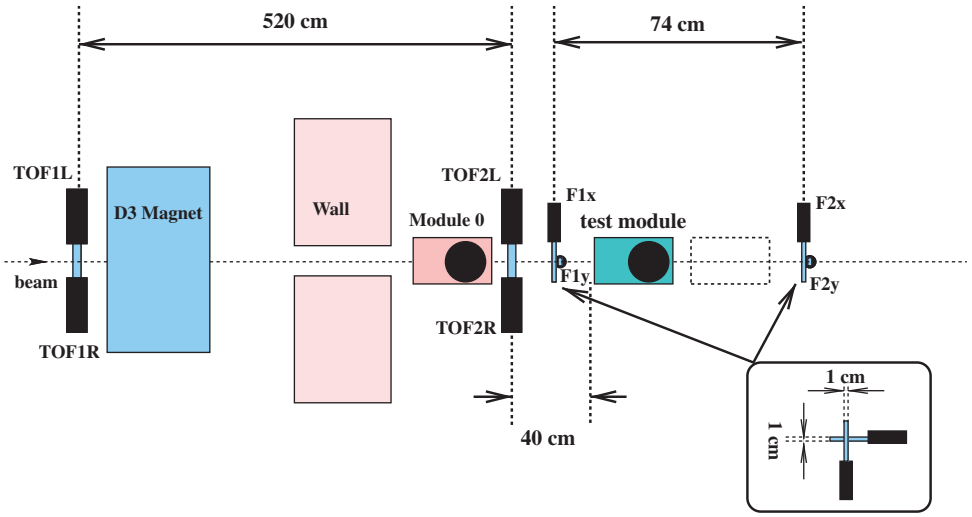

Fig. 6. Layout of the proton beam experiment. The module under test was placed at the position labeled "test module."

in the aerogel. Various loss factors such as geometrical acceptance and reflectivity of the optical system, quantum efficiency of the PMT, and the measured transmittance of the aerogel tiles were taken into account. (See the appendix for details.) The dips around $x = \pm 5$ cm are due to the boundaries between the aerogel tiles. The simulation successfully reproduces the measured photoelectron yield over the entire region. The absolute scale of the simulation was corrected so that the average photoelectron yield agreed with that of the data. This scale factor is the "calibration factor" and is found to be 0.55 for this module. The origin of this correction is due to uncertainty in the quantum efficiency of the PMT and deterioration of the aerogel surface during transportation and handling. In fact, fine fragments produced by frictional rubbing between the tiles were observed on the surface, and could cause an additional loss of the photoelectron yield.

2.3. Measurement of hadronic response

In this section, we describe test results with a proton beam. The purposes are to validate the MC simulation for hadronic interactions and to measure the detector responses to hadrons experimentally.

The experiment was performed at the 12 GeV Proton Synchrotron of the High Energy Accelerator Research Organization (KEK), Japan in 2002. Figure 6 shows the schematic layout. Figure 7 shows the test module with one 5 inch PMT and its parabola mirror. A 20 mm-thick lead converter and five aerogel tiles with the same dimensions as type-M and a total thickness of 55 mm were placed in the module. The aerogel used in this measurement had different optical characteristics from both type-M and type-A. Transmittance and calibration factor were separately measured for this aerogel. A much thicker converter than the reference configuration (Sect. 2.1) was used to enhance hadronic interactions. The trigger signal was formed by a coincidence signal from the time-of-flight counters (TOF1 and TOF2) and two 1 cm-wide mutually orthogonal counters (F1x and F1y). Particle identification was made by time-of-flight information measured by TOF1 and TOF2. A calibration factor was measured in a separate run using a 2.0 GeV/c π^+ beam with the lead converter removed.

Figure 8 shows the results of the measurement with MC expectation (GEANT3 [9] with the hadron package of GCALOR [10] and ray tracing scheme used in Sect. 2.2). The left figure shows an

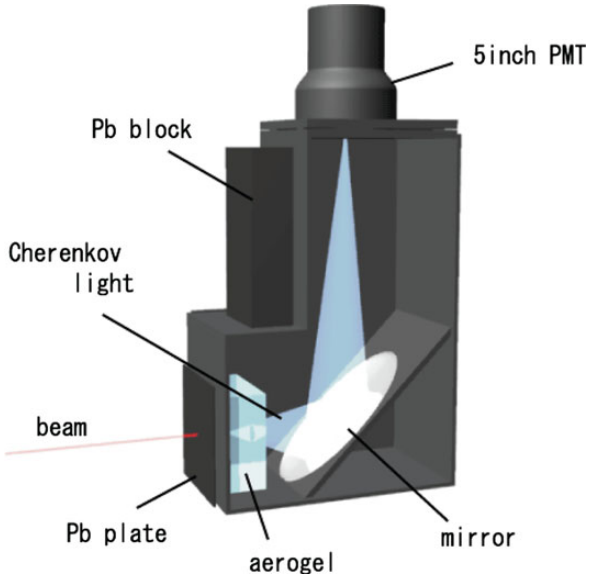

Fig. 7. Schematic view of the test module used in the proton beam experiment.

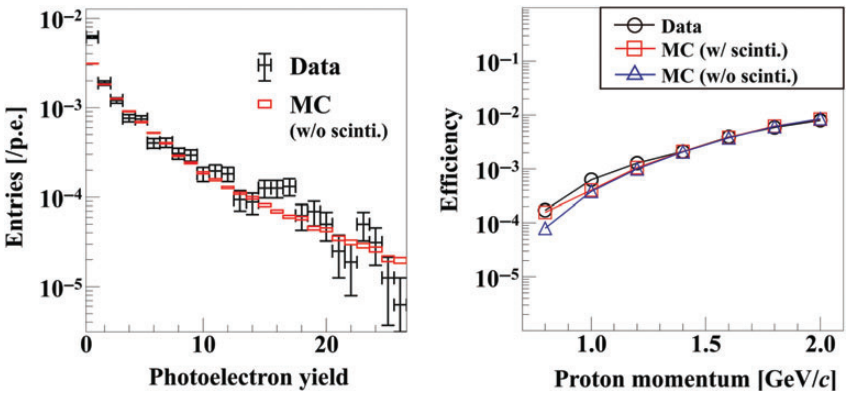

Fig. 8. (Left) Distribution of observed photoelectrons in the data and the MC for the 2.0 GeV/c proton beam. The vertical axis is normalized with the number of total triggered events. The simulation does not include the effects of nitrogen gas scintillation and the discrepancy is observed in the first bin. (Right) Detection efficiency for protons as a function of the momentum. Experimental results with a 1.75 p.e. threshold are shown with black open circles, with corresponding MC simulation results with and without a contribution from nitrogen gas scintillation by red open squares and blue open triangles, respectively.

example of photoelectron distribution and the right one shows the efficiency as a function of the proton momentum. Note that the efficiency obtained in this measurement is for a single test module. Despite the fact that a proton does not generate Cherenkov light in this momentum range, it can make a signal in the module through the generation of knock-on electrons and secondary particles such as π^0s. Additionally, scintillation light from nitrogen in air contributes to the light yield [11]. Figure 8 shows that the responses of this detector to protons are well understood. These results validate our MC simulations on the neutron blindness of the detector. Although the GEANT3 simulation was used here, it was confirmed that the same simulation with the GEANT4 code, which was adopted in other studies, reproduced this beam test result reasonably well; the largest discrepancy was at most a factor of 2, which was enough to predict the performance of this detector in the KOTO experiment.

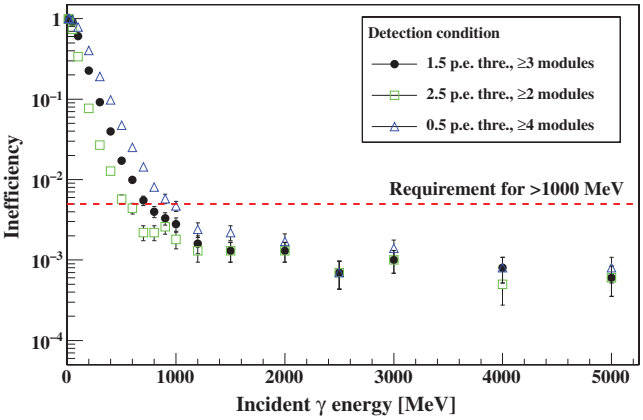

Fig. 9. Photon inefficiency of the BHPV detector estimated by MC simulations. Three different definitions for the photon hits are shown: ≥3 consecutive modules with >1.5 p.e. (black solid circles), ≥2 modules with >2.5 p.e. (green open squares), and ≥4 modules with >0.5 p.e. (blue open triangles). The red dashed line indicates the upper bound of the requirement described in Sect. 1.

2.4. Expected performance

In this section, we present the performance of the BHPV detector system evaluated with MC simulations, based on understanding the detector responses through a series of test experiments with a single module. GEANT4 simulation codes were used with the ray tracing scheme mentioned in Sect. 2.2. We focus on the photon efficiency and neutron blindness.

Condition of the simulation. The reference configuration described in Sect. 2.1 was used in the simulation study. The type-A aerogel, which is used in the KOTO physics run, was assumed, and the transmittance and calibration factors measured separately for this aerogel were implemented. The calibration factors were given as 0.8 for all modules, considering those for the 12 modules used in the physics run (Sect. 3) which were between 0.66 and 0.91. The simulation procedure is as follows. Photons with various energies were injected uniformly over the detector upstream surface in a 250 mm square. When $e^{\pm}$ tracks in the electromagnetic showers traversed the aerogel radiator, Cherenkov light was emitted and the rays were traced from the radiator to the PMT cathode. The amount of Cherenkov light at the PMT was converted to a number of photoelectrons by using the calibration factor. The same procedures were applied until all shower particles exited the entire detector or lost their energies completely.

Photon efficiency. The expected photon detection inefficiency as a function of incident energy is shown in Fig. 9 with black solid circles, for the reference configuration. The following algorithm was adopted to identify photons. In a single module, a hit was recognized when the output from either one of the two PMTs exceeded a 1.5 p.e. threshold. If three or more consecutive hits were recorded, then the event was identified as a photon. The simulation shows the photon efficiency requirement of the detector, >99.5% for >1 GeV, is satisfied.

Neutron blindness. An estimation of the neutron efficiency proceeded in the same way as the photon efficiency calculation. We used the hadron package of QGSP_BERT[12] to simulate the neutron interactions in the lead converter. All of the charged particles were tracked and Cherenkov light was

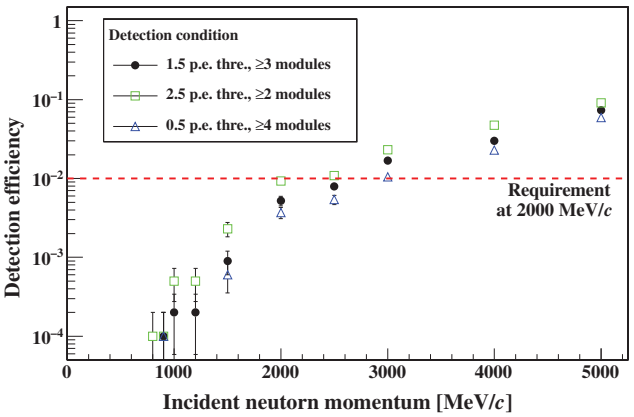

Fig. 10. Neutron efficiency of the BHPV detector estimated by MC simulations. The reference configuration is assumed. The meanings of the markers and the red dashed line are as in Fig. 9.

created when the momentum was above the Cherenkov threshold. The event identification algorithm was the same as in the photon case. Figure 10 shows the neutron efficiency as a function of incident neutron momentum. The efficiency increases monotonically with the momentum, and remains below 1% for 2 GeV/c neutrons, which is the requirement specified in Sect. 1.

Different algorithms may lead to different photon inefficiencies and neutron efficiencies. Examples of such studies are shown in Figs. 9 and 10. If the number of required consecutive hits is lowered, the efficiency for low-energy photons increases; however the efficiency for neutrons also increases. These conditions can be optimized according to specific experimental situations.

3. Photon identification in the neutral kaon beam

As mentioned in Sect. 1, part of the entire BHPV detector was installed in the experimental area together with the other detectors in the KOTO experiment. This partial detector consists of 12 modules, and was loaded with 58 mm-thick type-A tiles and lead converters with different thickness: five 1.5 mm (No. 1–5), five 3 mm (No. 6–10) and two with no plates (No. 11–12). Lead plates are unnecessary in the last two modules because they cannot produce photons that satisfy the criterion of hits in three or more consecutive modules. Outputs from this detector were recorded by 500 MHz waveform digitizers, which were custom-built for the KOTO experiment [13]. Multiple hits in a single counter were distinguished under high-rate environments.

We present analysis results from the 100-hour data set obtained in the first physics data-taking period in May, 2013. The beam power of the MR accelerator was 24 kW and gold was used as the production target, while the designed beam power was 291 kW with a nickel target. From beam-line simulations [14], the expected neutron and photon rates for kinetic energies greater than 1 MeV were 100 MHz and 170 MHz, respectively. We focus on the detector response to high-energy photons from K_L decays with the accompanied neutron and photon fluxes.

3.1. *Photon tagging with $K_L \to 3\pi^0$ decay samples*

There were six photons in the $K_L \to 3\pi^0$ decay. In the analysis, we required five out of the six photons to hit the CsI calorimeter. The kinematics of the decay allowed the reconstruction of the "missing" photon with a two-fold ambiguity. This "tagged photon" technique was used to evaluate the performance of the BHPV with the data collected in the KOTO experiment. We compared the data

with MC results to validate the performance. Here, the MC simulation included various K_L decay modes and interactions of daughter particles in BHPV as well as the other KOTO detectors. From this simulation, the "missing photon," denoted as γ_6 below, has a geometric acceptance of ∼3% in the direction of the BHPV. Details of the CsI calorimeter can be found elsewhere [2,15]. We started with the selection of the five reconstructed photons. For any two photons, when we assumed they were from π^0 decay, the longitudinal vertex position was calculated:

$$M_{\pi^0}^2 = 2e_1e_2(1-\cos\theta), \tag{1}$$

where M_{π^0} is the π^0 mass, θ is the opening angle, and e_1, e_2 were the photon energies. We further assumed the transverse position of the π^0 to be at the beam-line. Out of the five photons, there were 15 possible combinations to reconstruct two π^0 decays. For each of these 15 combinations, there were two vertices. We chose the correct combination by requiring the two vertices to be the same (best fit) so that it is the common vertex of the K_L decay. With the decay vertex known, the momentum of the third π^0 was calculated. We denote by γ_5 and γ_6 the two photons from the third π^0:

$$\begin{aligned} M_{\pi^0}^2 &= E_3^2 - \sum_{i=x,y,z} P_{3,i}^2 \\ &= (e_5+e_6)^2 - \sum_{i=x,y,z} (p_{5,i}+p_{6,i})^2 \\ &= \left(e_5 + \sqrt{p_{6,x}^2+p_{6,y}^2+p_{6,z}^2}\right)^2 - \sum_{i=x,y,z} (p_{5,i}+p_{6,i})^2, \end{aligned} \tag{2}$$

where E_3, e_5, and e_6 are the energies of the third π^0, γ_5, and γ_6, respectively. The $P_{3,i}$, $p_{5,i}$, and $p_{6,i}$ ($i = x, y, z$) are the i components of the momenta. For the three unknowns of the γ_6 momenta, the two transverse components ($p_{6,x}$, $p_{6,y}$) were determined by assuming that the parent K_L has no transverse momentum. Equation (2) is therefore quadratic in $p_{6,z}$. For the two solutions of $p_{6,z}$, we obtained two K_L invariant masses. The solution with the larger (smaller) $p_{6,z}$ was called the "forward"("backward") solution and the corresponding K_L mass was denoted as $M_{K_L}^{\rm forward}$ ($M_{K_L}^{\rm backward}$).

We required $480 < M_{K_L}^{\rm forward} < 570\,{\rm MeV}/c^2$, because a simulation study showed that the forward solution was correct for most of the cases in which γ_6 hit the BHPV detector. Events with $480 < M_{K_L}^{\rm backward} < 525\,{\rm MeV}/c^2$ were rejected to reduce unnecessary backward solution events. Comparison of the $M_{K_L}^{\rm forward}$ distribution between the data and MC is shown in Fig. 11. The MC result was normalized with the number of events after the cuts on the reconstructed K_L mass. The MC well reproduced the data, though the distribution had no clear peak around the nominal K_L mass due to events with incorrect photon combinations. When we selected the events with proper photon combinations and γ_6 pointing to BHPV in the simulation, the distribution had a peak around the nominal K_L mass, shown as the blue histogram in Fig. 11. The background contamination, mainly from $K_L \to \pi^+\pi^-\pi^0$ and $K_L \to 3\pi^0$ decays with subsequent Dalitz decay ($\pi^0 \to e^+e^-\gamma$), was estimated to be 9.8%.

As a reference, events where all the six photons from the $K_L \to 3\pi^0$ decay hit the calorimeter were reconstructed. These events were called "6γ" events, and the reconstruction was almost the same as 5γ events other than the assumption that all $3\pi^0$ came from the common decay vertex. With the same normalization factor as in Fig. 11, the number of 6γ events was found to be consistent between the data and MC within a statistical uncertainty of 0.5%.

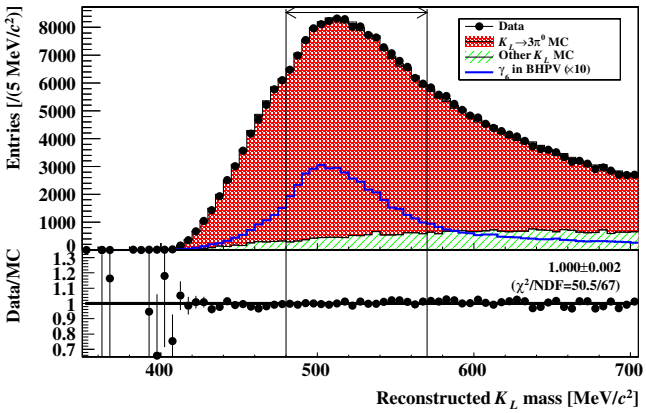

Fig. 11. Invariant mass distribution of the 5γ events with the forward solution. The selection on $M_{K_L}^{\text{backward}}$ is applied. In this plot, the $K_L \to 3\pi^0$ MC (histogram in red) includes the subsequent $\pi^0 \to e^+e^-\gamma$ decays. The blue histogram (scaled up by 10) is for events with the correct combination and γ_6 going into the BHPV detector. The lines and arrow indicate the selection region.

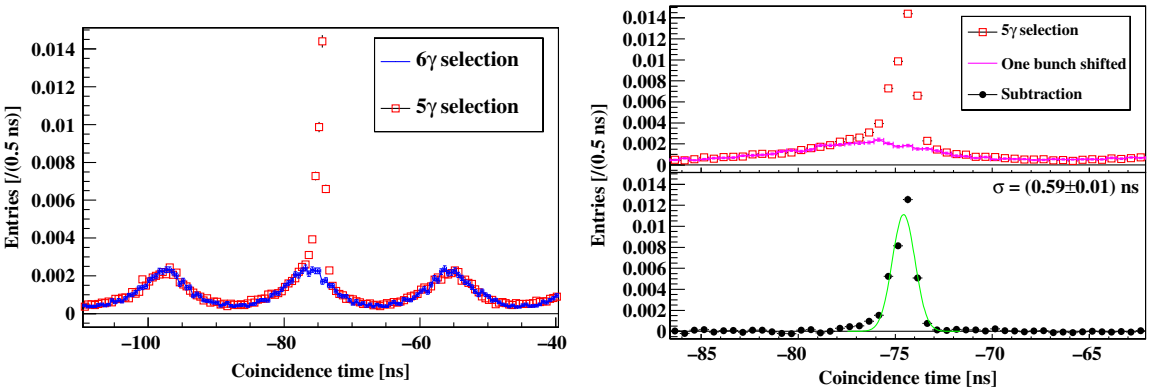

Fig. 12. (Left) Timing distribution of the BHPV hit events for the 5γ (red) and 6γ (blue) selections. (Right top) Timing distribution of the 5γ events between -86.6 and -62.6 ns (red) and the events in the previous bunch (between -107.8 and -83.7 ns) shifted by a cycle of 21.1 ns (purple). (Right bottom) Time distribution of the 5γ events after subtracting the distribution of accidentals in the previous bunch. The line is a Gaussian fit result and the obtained σ value is written in the right corner.

3.2. BHPV photon response

We examined the response of the BHPV detector by using the 5γ and 6γ events. A photon hit in the detector was identified as three or more consecutive modules with outputs exceeding the 2.5 p.e. threshold in either or both of the left and right PMTs. Figure 12 shows the timing distribution of the photon hits in the BHPV detector with respect to the timing determined by the CsI calorimeter. The BHPV hit timing was defined as the hit times averaged over the modules with hits after correcting the time of propagation of the shower particles module by module. The CsI hit timing was the weighted average of the photon hit times where the weight is given by the photon energy. Correction due to the time of flight between a decay vertex and the hit positions was applied. For the 6γ events, shown with the blue bars in Fig. 12 (left), there should only be accidental hits in the BHPV detector. The periodic distribution reflects the beam structure in the slow extraction beam from the J-PARC MR. On the other hand, for the 5γ events shown by the red open squares, a sharp peak is observed on top of the accidental hits. It clearly shows that the missing photons tagged by the 5γ events were

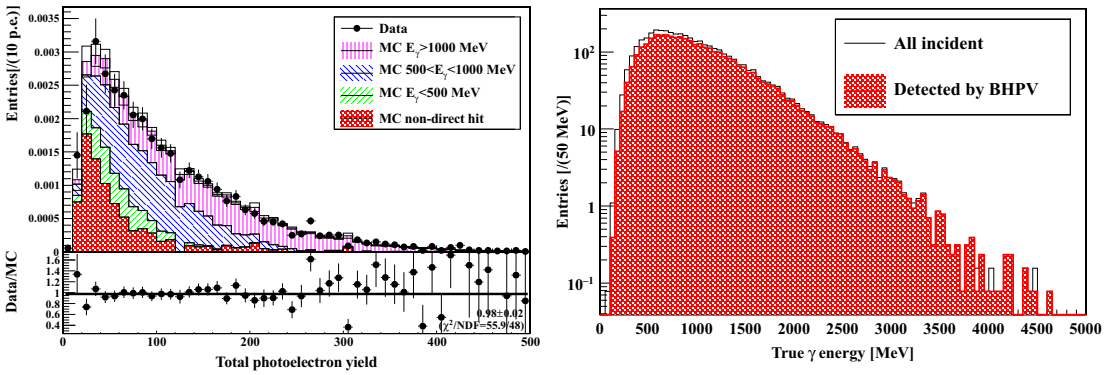

Fig. 13. (Left top) Distribution of the total photoelectron yield. The solid points show the real data while the histograms show the MC simulation results. The energies of the missing γ in the MC are classified by colors: 0–500 MeV (green), 500–1000 MeV (blue), 1000 MeV or more (yellow), and other events (red) in which photon conversion points are outside the BHPV detector (non-direct hits). The open box on each bin indicates the statistical error of the MC data. (Left bottom) Ratio of the real data to the MC data. (Right) Distribution of the γ_6 energy in the MC simulation.

successfully detected by the BHPV detector. Figure 12 (right bottom) shows the timing distribution of the 5γ events after subtracting the distribution of the accidental hits in Fig. 12 (right top). The σ value from the Gaussian fit was found to be 0.59 ns, which was slightly larger than expectation from calorimeter and BHPV timing resolution. The difference comes from accidental hits and further studies are needed to understand these effects.

We compared the number of events within ± 7.5 ns of the peak in the timing distribution of the 5γ events between the data and MC. Figure 13 (left) shows the distribution of the total photoelectron yields observed by the hit modules in these events. The total photoelectron yield was obtained by summing the outputs over the modules which recorded hits in three or more consecutive modules. Here, the output from a module was defined as the sum of the outputs exceeding 2.5 p.e. for the left and right PMTs. For the data and MC, distributions of the accidental hits were subtracted. The data and MC distributions agree. As expected, the photoelectron yields increase with the energies of the γ_6 (the missing photon). The energy distribution of the γ_6 going in the BHPV direction in the simulation is shown in Fig. 13 (right). We now focus on the events with total photoelectron yield greater than 200 to examine the response against high-energy photons. $N_{\rm data}$ and $N_{\rm MC}$ were defined as the numbers of such events in the real data and the MC simulation, respectively. In addition, we define $\eta = N_{\rm data}/N_{\rm MC}$. Since the MC simulation shows that these events are mainly from the γ_6 with >1000 MeV hitting the detector (90.3%), η is a good measure of the detector response to high-energy photons. If the detector works as expected, η should be close to 1. From Fig. 13, $\eta = 1.025 \pm 0.050 \pm 0.068$, where the first and second errors represent statistical and systematic uncertainties, respectively. A summary of the systematic errors is presented in Table 2. The MC reproducibility of the BHPV responses was evaluated by comparing the efficiency of each selection cut related to the BHPV between the data and MC. For other error sources, each condition was shifted within its uncertainty in the MC simulations and changes of the geometrical acceptance of γ_6 in the BHPV were considered as the error.

Finally, the detection efficiency for high-energy photons was estimated from the η value obtained above. The efficiency was defined as

$$\epsilon'_{\rm data} = N'_{\rm data}/N'_{\rm incident}, \tag{3}$$

Table 2. List of systematic uncertainties.

Error source	Relative error [%]
BHPV responses	3.80
K_L momentum spectrum	$^{+1.70}_{-1.35}$
Beam position	0.15
Calorimeter energy resolution	0.49
Calorimeter position resolution	4.98
Detector alignment	1.50
Total	$^{+6.68}_{-6.60}$

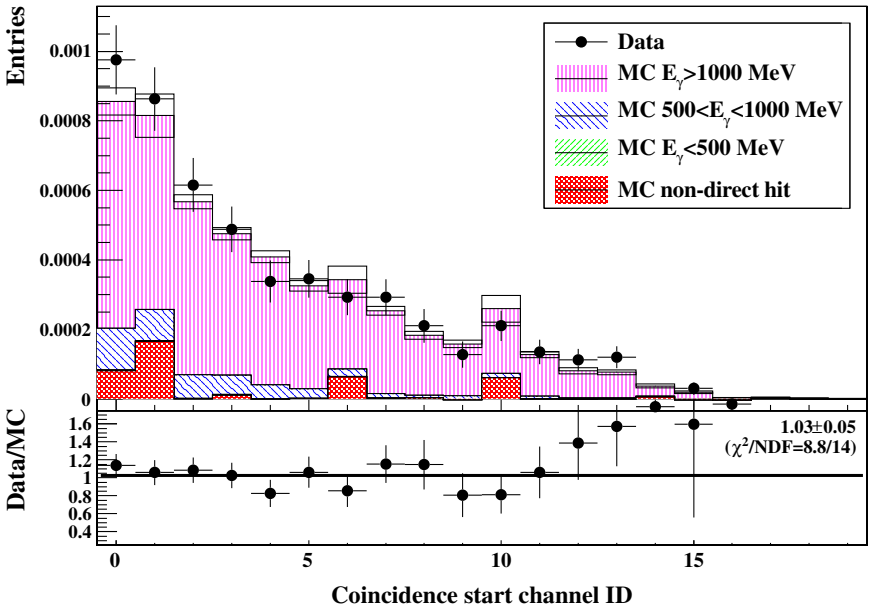

Fig. 14. (Top) Distribution of the shower starting module in the events with a total photoelectron yield larger than 200. The solid points show the real data while the hatched histograms show the MC simulation result. See Fig. 13 for the color codes. (Bottom) Ratio of the real data to the MC data.

where variables with a prime ($'$) indicate that the incident γ energy is larger than 1 GeV. $N'_{\rm data}$ and $N'_{\rm incident}$ are the numbers of events with γ_6 detected in or incident on the BHPV detector, respectively. We assumed

$$\frac{N_{\rm data}}{N'_{\rm data}} \simeq \frac{N_{\rm MC}}{N'_{\rm MC}}, \tag{4}$$

and evaluated $N'_{\rm incident}$ with the simulation. This assumption allows Eq. (3) to be restated as follows:

$$\begin{aligned}\epsilon'_{\rm data} &\simeq (N'_{\rm MC}/N_{\rm MC} \times N_{\rm data})/N'_{\rm incident} \\ &= \epsilon'_{\rm MC} \times \eta.\end{aligned} \tag{5}$$

The efficiency in the MC simulation, written as $\epsilon'_{\rm MC}$, was calculated to be 0.938 ± 0.002(stat.). Here, the inefficiency of $\sim$6% mainly came from lack of the total radiation length and would be reduced by adding modules to increase the thickness of the lead converter. From Eq. (5), the efficiency for high-energy photons was obtained as $\epsilon'_{\rm data} = 0.962 \pm 0.046(\text{stat.})^{+0.064}_{-0.063}(\text{syst.})$.

The η value, which indicates the reproducibility of MC, is consistent with the value 1.0 within error. We conclude that high-energy photons are successfully detected by this detector as expected when it was placed in the intense neutral beam. The agreement between data and MC in distribution of the shower-starting module in Fig. 14 further confirms the detector performance. The obtained efficiency, which is close to 1.0, validates the excellent performance of BHPV as a photon veto detector.

4. Summary

In this paper, we described a novel photon detector used in an experiment with an intense neutral kaon beam line. Aerogel Cherenkov radiation is used for the detection of electromagnetic showers. It has the advantage that it is neutron blind. According to MC simulations, validated by test experiments with positrons and protons, efficiencies for photons with energies larger than 1 GeV and for neutrons with a momentum of 2 GeV/c are $> 99.5\%$ and $< 1\%$, respectively. The detector was partially installed in the first physics run of the KOTO experiment, and the performance for high-energy photons was evaluated by tagging $K_L \to 3\pi^0$ decay events. Within an 8.2% uncertainty, which was obtained as the quadratic sum of statistical and systematic errors, the photon detection efficiency was found to be consistent with MC expectation. In order to achieve higher efficiency with a more intense beam, we plan to change the configuration by adding more modules and optimizing the sampling of lead and aerogel according to the beam condition.

Acknowledgements

We would like to express our gratitude to the staffs of the KEK Proton Synchrotron and the Laboratory of Nuclear Science for their cooperation in the test beam experiments. We also thank the staff members of the J-PARC accelerator, Hadron Beam groups, and the KEK Computing Research Center for their support in taking and analyzing the physics data. Part of this work was supported by JSPS/MEXT KAKENHI Grant Numbers 23224007, 18071006, 14046220, and the Japan/US Cooperation Program. Some of the authors were supported by Grant-in-Aid for JSPS Fellows.

Appendix: Aerogel transmittance measurement

The transmittance of aerogel is known to be influenced mainly by two effects: absorption and Rayleigh scattering. According to [16], it can be represented as

$$T(\lambda) = \exp(-\alpha \Delta x) \exp\left(-\frac{C \Delta x}{\lambda^4}\right), \tag{A1}$$

where Δx and λ denote the thickness of the aerogel and the wavelength of the light, respectively. α and C are constants. The first (second) exponential represents the absorption (Rayleigh scattering) effect, and α and C characterize the aerogel's transmittance property.

These constants were measured using the setup shown in Fig. A1. There were five LEDs with different colors, which were irradiated onto the aerogel sample under test through 2 mm-diameter holes. The LEDs and aerogel sample were placed on movable tables controlled by a computer. The transmittance was obtained by comparing light outputs from the main PMT behind the aerogel sample and those without the sample. The stability of the LEDs was monitored by a separate PMT placed near the LEDs. An example of the measurement results is shown in Fig. A2 together with a fit result with Eq. (1). In Table A1, we list the parameters obtained for the type-A and type-M aerogels averaged over many measurements and samples. Combined with the information from the photoelectron calibration experiment, these parameter measurements provide inputs to the simulation studies.

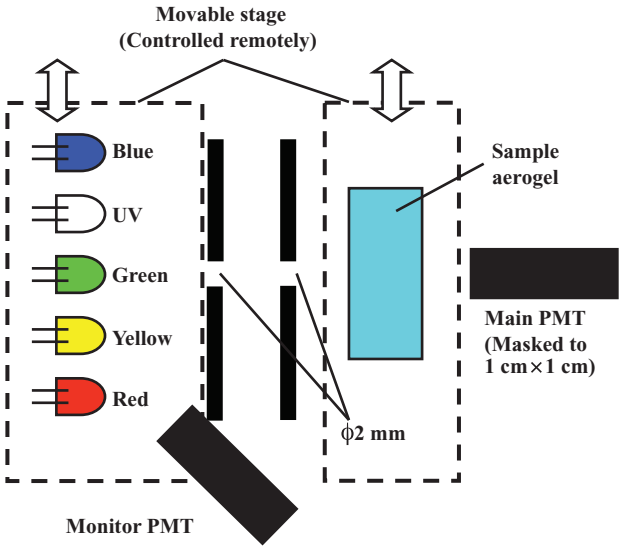

Fig. A1. Layout of the aerogel transmission measurement. The section inside the broken lines can be moved remotely.

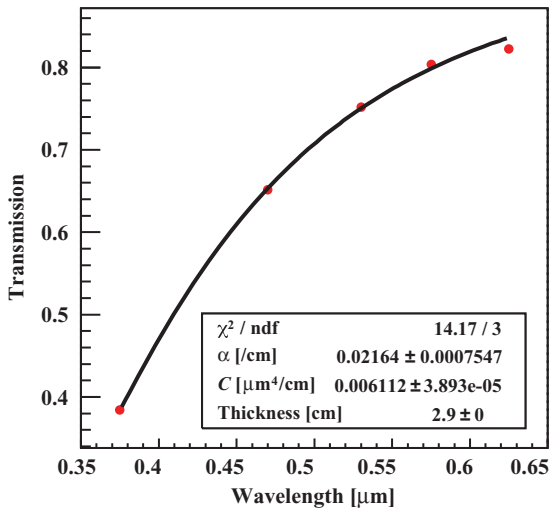

Fig. A2. Results of the aerogel transmission measurement.

Table A1. Summary of transmittance measurements.

Type	A^*	C [$\mu m^4\,cm^{-1}$]
M	0.96	0.0040
A	0.972	0.00692

*The parameter A is defined as $A = \exp(-\alpha \Delta x)$, where Δx is 1 cm.

References

[1] J. Comfort et al., J-PARC E14 (KOTO) experimental proposal, http://koto.kek.jp/pub/p14.pdf, date last accessed May 21, 2015.
[2] T. Yamanaka, Prog. Theor. Exp. Phys. **2012**, 02B006 (2012).

[3] T. Koseki et al., Prog. Theor. Exp. Phys. **2012**, 02B004 (2012).
[4] J. Brod, M. Gorbahn, and E. Stamou, Phys. Rev. **D83**, 034030 (2011).
[5] S. Fukui et al., Workshop on Hadron Physics at e^+e^- Collider, 38 (1994).
[6] M. Tabata et al., Nucl. Instrum. Methods **A668**, 64 (2012).
[7] R. Winston, J. Opt. Soc. Amer. **60**, 245 (2004).
[8] S. Agostinelli et al., Nucl. Instrum. Methods **A506**, 250 (2003).
[9] C.P.L.L.W. W5013: GEANT – Detector Description and Simulation Tool, 1993.
[10] C. Zeitnitz, and T. A. Gabriel., Nucl. Instrum. Methods **A349**, 106 (1994).
[11] H. Morii et al., Nucl. Instrum. Methods **A26**, 399 (2004).
[12] S. Banerjee, J. Phys.: Conf. Ser. **331**, 032002 (2011).
[13] M. Bogdan, J-F. Genat, and Y. W. Wah, Proc. 17th IEEE NPSS Real Time Conference (RT), 1–2, (2010).
[14] T. Shimogawa, Nucl. Instrum. Methods **A623**, 585 (2010).
[15] T. Masuda, PhD thesis, Kyoto University (2014).
[16] E. Aschenauer et al., Nucl. Instrum. Methods **A440**, 338 (2000).